



The spark plasma sintering of the optimized parametric process for the magnesium alloy reinforced hybrid nano-ceramics

Juwon Fayomi^{1,2} · Abimbola Patricia Popoola^{1,2} · Olawale Popoola³ · Victor Aigbodon^{1,4} · Oluranti Agboola^{1,5}

Received: 4 September 2022 / Accepted: 28 November 2022 / Published online: 6 December 2022
© The Author(s), under exclusive licence to Springer-Verlag London Ltd., part of Springer Nature 2022

Abstract

A novel hybridized magnesium-based metal matrix composite consolidated with 4wt% AlN-4wt% Y_2O_3 -4wt% VB nano-ceramics has been developed via powder metallurgy (PM) of spark plasma sintering (SPS) process. A statistical Taguchi design was employed to examine the significant effects of the individual or the interactive sintering parametric process, namely, sintering temperature, pressure, dwell time, and heating rate on the relative density, hardness, and nanohardness of the developed composite. The outcome of the optimized process shows that all the factors contributed to the densification and hardness of the composite, but temperature was seen as the major factor that significantly influenced the process beyond 90%. The highest microhardness value of 106 HV and 2.8 GPa nanohardness was exhibited by the material sintered at 500 °C, 40 MPa of pressure, 5 min of dwell time, and a heating rate of 100 °C/min. Likewise, a minimum crystallite size of 8.87 nm and the smallest grain size of 17.68 μm were achieved at the highest sintering temperature. However, the modeling response suggested that full densification (relative density of about 99%) can be achieved at sintering temperature of 500 °C, pressure of 30 MPa, dwell time of 5 min, and heating rate of 75 °C/min.

Keywords Spark plasma sintering · Relative density · Ceramics · Nanohardness · Taguchi design · Microstructure

1 Introduction

In recent times, rapid evolution has been recorded for the exploration of novel lightweight materials for structural engineering applications. These continuous innovations mostly in the transportation sectors are to manufacture sustainable and green components that are lightweight and energy-efficient. In lieu of the abovementioned objectives,

magnesium and its alloys emerge as a suitable replacement for conventional materials. Industrially, magnesium alloy has established an important impact courtesy of its low density, excellent weight-saving capacity, low working temperature, and good stiffness [1, 2]. Unfortunately, the lightweight prowess of magnesium alloy is not enough to position them as a material of choice where high-temperature materials are required since they are limited with poor mechanical strength, corrosion-prone, and highly unstable under aggressive environments or temperatures [3, 4]. The established limitation has made the commercialization of magnesium to be difficult.

So far, AZ91D magnesium-based alloy has been asserted as a new adventurous material owing to its distinctive attributes like a better young modulus, low density, good capacity of damping, and low thermal coefficient of expansion [5–7]. These super properties have made them an applicable material in most industries such as auto-engines, aircraft brakes, auto rims and wheels, and medical implant devices [8–10].

Hence, the need to optimize magnesium alloy by alloying with other elements or reinforcing with particulate to form a composite becomes essential. Therefore, the incorporation of highly stable particles like ceramics in nanoscale is highly

✉ Juwon Fayomi
fayomi_chris@yahoo.com; 218749836@tut4life.ac.za

¹ Department of Chemical, Metallurgical, and Materials Engineering, Tshwane University of Technology, P.M.B. X680, Pretoria, South Africa

² Surface Engineering Research Laboratory, Tshwane University of Technology, P.M.B. X680, Pretoria, South Africa

³ Department of Electrical Engineering, Tshwane University of Technology, P.M.B. X680, Pretoria, South Africa

⁴ Department of Metallurgical Engineering, University of Nigeria, Nsukka, Nigeria

⁵ Department of Chemical Engineering, Covenant University, Ota, Nigeria

sorted after as they render super strength to magnesium alloy both at ambient and at elevated temperatures, improve hardness, enhance creep, and corrosion resistance [11, 12].

Aside from the ability of different ceramics to improve properties, the particulate size of the ceramics also serves an essential role in determining the extent and degree of properties' enhancement. Records have shown that matrix reinforced with micron-size particles often causes wettability deficiency in which gaseous air is likely trapped along the grain boundaries and forms deformation such as clustering, agglomeration, and or porosity [13, 14].

With the emergence of nanotechnology, efforts were made to narrow down the micron-sized materials to nano-sized particles to curb the poor wettability and as well enhance the strengthening mechanism of the material's behavior. It has been reported in the open literature that less than 2% of nano-sized particles in a composite have the potential of influencing with excellent properties [15].

Sankaranarayanan et al. [16] have proven that the presence of nano reinforcement can improve the marginal grain refinement, enhance the tensile strength, and reduce the coefficient of thermal expansion. This assertion was reached when nano AlN particles at varying percentage weight composition (0.2%AlN and 0.8%AlN) were introduced into the matrix of magnesium alloy using the microwave-assisted and hot extrusion process. The outcome of the research revealed improved properties of the composite compared to the monolithic Mg alloy.

Nevertheless, the strength enhancement of the monolithic Mg alloy solely depends on the degree of even distribution of the second phase in the matrix which can only be determined by optimizing the manufacturing parameters of the employed technique. Likewise, other ceramic particulates like SiC [17–19], nanoplatelet graphene [20–22], Y_2O_3 [23, 24], TiO_2 [25, 26], TiB_2 [27–29], W C [30–32], and Si_3N_4 [33, 34] have been employed to reinforce monolithic magnesium alloys, and excellent properties have been obtained.

Powder metallurgy route [1, 5, 35–37], stir casting process [38, 39], friction stir welding [40, 41], coating [42, 43], squeeze casting [44], and disintegrated melt deposition [45] are some of the major techniques employed to develop, fabricate, and synthesize magnesium-based composites with enhanced properties. Somewhat, the fabrication of nano-reinforced composite can be difficult due to the proximity to agglomeration and poor wettability if the parameters and the technique are not well selected and controlled. Moreover, cost-effectiveness, accessibility, availability, flexibility, and environmental and economic implications are some of the major factors considered before selecting any fabricating technique.

Undoubtedly, the spark plasma sintering (SPS) process has proven to be exceptional powder metallurgy (PM) method of fabricating nanostructured ultrafine-grained

materials owing to their flexibility in manufacturing complex shapes, absence of possible chemical reactions that might emanate between the matrix and the reinforcing phase, ability to produce a highly dense consolidated solid materials with good bonding structure, and barrier to the coarsening of grains [34, 46]. In SPS process, solid bulk materials can be consolidated at a low temperature and permit the inclusion of a larger weight percentage of particles that are conventionally impossible to manufacture by other processing means.

Several composites have been developed successfully using the PM process, and high densification to excellent properties was achieved [1, 4, 35–37]. Dodi et al. [47] sintered high-temperature ceramics ZrB_2 –SiC– HfB_2 to investigate the influence of the sintering parameters on the oxidation resistance of the materials. The results show that the oxidation resistance decreases with increasing temperature. Likewise, Cohen et al. [48] examined the effect of the heating rate and specimen thickness on the behavior of magnesium aluminate using SPS, and the outcome revealed that the highest sample thickness can be achieved at a low heating rate. A spinel ceramic of magnesium aluminate was reinforced with isobutylene-maleic anhydride (ISOBAM) via the SPS route; the composite was admixed at 85 wt.% of the primary matrix and 0.7 wt.% of ISOBAM. The results show a high density of 99.97% with a reduced pore space as reported by Shahbazi et al. [49].

However, research on the preparation of magnesium-based composite by powder metallurgy and the evolution of microstructure and mechanical properties is limited in the open literature.

In this present research, hybrid vanadium boride (VB), aluminum nitride (AlN), and yttrium oxide (Y_2O_3) ceramic-reinforced Mg–Al–Zn alloy was developed using the spark plasma sintering process of powder metallurgy. Aluminum nitride (AlN) is a ceramic particulate with a high melting point of 2200 °C, 273–346 GPa elastic modulus, and a density of 3.26 g/cm³. It is characterized by strong thermal stability, high conductivity, and moderate thermal coefficient of expansion [16]. Experimental works have been reported on the influence of nano AlN as a promising reinforcement in metal alloys, and the results show an improvement in hardness, tensile strength, and compressive strength [50–53]. Similarly, the thermodynamically stable yttrium oxide (Y_2O_3) with a melting temperature of 2425 °C is an essential refractory material. The incorporation of this hard-ceramic material into the alloys has been affirmed by researchers to provide enhanced mechanical and tribological properties [13, 54]. Moreover, VB is a promising boride of a transition metal vanadium that is utilized as a cutting tool and a wearable resistance material which is a function of its high mechanical and thermal properties. The microstructural behavior and mechanical performance

of VB reinforced composite at the varying weight percentage of 1, 2, and 5% using a PM route were studied by [55]. The outcome shows the absence of an intermetallic phase, and a low failure strain was observed with the reinforced composite. However, no single known report to the authors on the manufacturing of a quaternary Mg-4wt%AlN-4wt%Y₂O₃-4wt%VB composite via the PM route. Therefore, the present studies entail the fabrication of a novel hybrid Mg-4wt%AlN-4wt%Y₂O₃-4wt%VB using the spark plasma sintering route to investigate the effect of the sintering parameters viz., sintering temperature, pressure, dwell time, and the heating rate on the relative densification, microhardness, and nanohardness. It is important to state that the outcome of the properties is a function of the combined factorial effect of sintering parameters.

2 Materials and methods

2.1 Experimental materials

In this study, powder of magnesium alloy AZ91D supplied by Dome Metal Co. Ltd. China with 99.95% purity, 1.738 g/cm³ density, and particle size of 15–53 μm was employed as the primary matrix material. Aluminum nitride (AlN) of 100–200 nm (99.9% purity) and yttrium oxide (Y₂O₃) of 40 nm (99.9% purity) were supplied by Hongwu International Group Ltd., China, and vanadium boride (VB) of 100–200 nm (99.9% purity) that was supplied by Liche Opto Group Co., Ltd., China, was utilized as the reinforcement at an equal mixing ratio of 4% wt. each.

Mg-4wt%AlN-4wt%Y₂O₃-4wt%VB were measured into a container and subjected to a dry mixing procedure by using a tubular mixer at 150 rpm for 12 h to achieve homogeneity of composite material. Prior to the commencement of the mixing process, 8-mm steel balls of 2:5 powder-to-ball ratio were placed in the powder container to ensure proper inclusion of the reinforcing particulate in the primary matrix.

2.2 DOE

Design of experiment (DOE) has been established as an essential tool for collecting, analyzing, and interpreting data to obtain an optimum experimental outcome. Fundamentally, the process of DOE is carried out to derive the best parametric factors that determine the results and their influence on the response desired.

Owing to the challenges posed by the traditional methods of optimizing an experimental procedure, the Taguchi route, factorial design, and response surface methodology were invented and widely used to replace conventional techniques. Among all, Taguchi has been greatly employed to optimize the parametric process of an experiment due to

the possibility of reducing the experimental runs and minimizing the cost of production. The Taguchi process entails the orthogonal array (OA) which is the rows and columns that accommodate the possible combination of variable runs [56]. Likewise, it contains the signal-to-noise ratio (S/N), in response to the factorial and level variables that help reduce the effect of noise and give the maximum features of the end products by increasing the S/N ratio. The S/N ratio can either be smaller is best, larger is best, or nominal is best depending on the degree of deviation from the desired response.

Generally, this design is characterized by system design, tolerance design, and parametric design. The system design aided the selection of the factors and adequate levels in any experimental design. The tolerance design modifies the outcome of the parametric design by adjusting the tolerance factor, while the performance behavior of the factorial design that involves the identification of the optimum description, and reduction in experimental noise is done by the parameter design.

2.3 Procedure of Taguchi design route in this study

Generally, the best experimental research is conducted following the orthogonal array (OA) at standard because of the ability to identify or uphold the required variables at the maximum level and delete the unwanted combined variables. Therefore, in this novel research, the Taguchi method is selected over the factorial design since it saves time by decreasing the number of experimental runs. Using OA, L9 3⁴ (nine experimental runs) was generated as seen in Table 1.

Four (4) factor variables viz. (A) temperature (450, 475, 500 °C), (B) pressure (30, 40, 50 MPa), (C) dwell time (5, 10, 15 min), and (D) heating rate (50, 75, 100 °C/min) were employed in this research at three different levels. In addition, relative density, nanohardness, and microhardness were set as the response variables. ANOVA software in Minitab 19 was utilized to test the parametric process significance.

For easy connotation in this study, the experimental runs are represented as a, b, c, d, e, f, g, h, and i.

Table 1 The selected factors and levels for the experiment

Parameters	S.I. units	Symbol	Level 1	2	3
Temperature	(°C)	A	450	475	500
Pressure	MPa	B	30	40	50
Dwell time	min	C	5	10	15
Heating rate	°C/min	D	50	75	100

2.4 The procedure of spark plasma sintering process

In this study, the blended admixed powders (Mg-4wt%AlN-4wt%-Y₂O₃-4wt%VB) in equal weight proportions were consolidated using the spark plasma sintering machine of model SPS FCT Systeme GmbH, Germany. The measured quantity of the admixed particulates was poured into a 40-mm graphite die with the appropriate punches. Before pouring the powder into the graphite die, a graphite sheet was placed to ensure spacing between the inner wall of the die and the powder. This was done to enable the smooth removal of the consolidated powder after the sintering process and well minimize the gradient temperature on the workpiece. The samples were sintered according to the design in Table 2.

Following the removal of the sintered samples from the graphite die, they were sandblasted to remove the graphite impurities and then subjected to metallographic treatment by cutting, grinding, and polishing.

2.5 Characterization and analysis of the sintered samples

2.5.1 Density analysis

A densitometer that functions relatively on Archimedes principles was utilized to determine the individual density of the sintered composite. The measurement was done repeatedly about 7 times, and the average was reported as the mean experimental density. Likewise, the rule of the mixture as stated in Eq. 1 was used to calculate the theoretical density. The relative density of the composite and percentage porosity which are derived from the experimental density was evaluated with Eqs. 2 and 3:

$$\text{Theoretical density} = \frac{1}{\frac{\%MgAZ91D}{\rho_{MgAZ91D}} + \frac{\%AlN}{\rho_{AlN}} + \frac{\%Y2O3}{\rho_{Y2O3}} + \frac{\%VB}{\rho_{VB}}} \quad (1)$$

$$\text{Relative density} = \left(\frac{\text{Experimental density}}{\text{Theoretical density}} \times 100 \right) \% \quad (2)$$

$$\text{Percentage porosity} = 100\% - \text{Relative density} \quad (3)$$

2.5.2 Microstructure and crystalline phase characterization

The microstructural modification of the sintered samples was done using an optical microscope (OM) (Olympus BX 51 TRF, Japan). Prior to the characterization, the samples were dimensioned to 10 by 10-mm size, grinded with emery papers, and polished to a mirror-like surface. The OM revealed the grain boundaries (neck formation) as contained in each of the designed samples. Also, the crystalline phase and compound present in the samples were examined using X-ray diffraction (XRD) at a wavelength of 1.5406 and K-alpha of 0.94. To understand the crystallite size that is present in each sample at the nanoscale, the Scherrer formula was employed as shown in Eq. 4:

$$\tau = \frac{K\lambda}{\beta \cos\theta} \quad (4)$$

where K is the Scherrer constant, λ is the wavelength of the x-ray source with a value of 0.15406; β is the full width half maximum FWHM measured in radians; θ is the Bragg's angle measured in radian. τ is the crystallite mean size.

2.5.3 Microhardness and nanohardness

The Vickers microhardness of the nano-sintered composite was investigated using the Vickers tester of model FM-800, Japan. The tester is made up of a diamond indenter, and the polished samples were loaded with 100 g force for 15 s of dwell time at 0.5-mm spacing. Averagely, 7 indentations were taken on both the matrix and the reinforced phase, and the effective mean hardness was calculated.

To further elucidate the mechanical properties of the composite, the samples were subjected to a nanomechanical tester using the nanoindenter (NHT, Switzerland). Berkovich diamond with pyramidal 3-sided shape was used as the indenter on a polished mirror surface. One hundred millinewton was applied to the samples at 10 mN/min of loading and unloading rate. In this study, nanohardness is specifically considered, and it was examined based on the ratio of the maximum load (F_{\max}) to the area of contact (A_c) of the sample. The nanohardness of the materials is expressed in Eq. 5:

Table 2 Experimental design

Experimental samples	Temperature (°C)	Pressure (MPa)	Dwell time (min)	Heating rate (°C/min)
a	450	30	5	50
b	450	40	10	75
c	450	50	15	100
d	475	30	10	100
e	475	40	15	50
f	475	50	5	75
g	500	30	15	75
h	500	40	5	100
i	500	50	10	50

$$H_N = \frac{F_{\max}}{A_c} \quad (5)$$

3 Results and discussion

3.1 Microstructural study of the sintered samples

The microstructure of the sintered materials at varying parameters is presented in Fig. 1. As observed in Fig. 1a–c for the materials sintered at the same temperature, the neck which depicted a strong bonding at the grain boundaries has not been formed completely. Hence, this resulted in low density as experimented. Nonetheless, Fig. 1b shows less porosity and moderate bonding structure. Thus, the displayed structures in Fig. 1a–c show that there was no diffusion of the reinforcing particulates during the spark plasma

sintering process at those parameters. Fig. 1d reveals the emergence of the neck formation, the initiation of plastic deformation of the material, and the refinement of particulates along the grain boundaries. Although, the formation breaks in Fig. 1e and a structure with loose bonding was formed despite sintering at the same temperature as Fig. 1d and f. This is proof that all other parameters also play a significant role in determining the nature of the microstructure of a sintered material. The spherical structure of the AZ91D matrix is well revealed in Fig. 1d and f with suitable adhesion of the reinforcing phase at the grain boundaries. The observed low pore space and higher densification experienced could be the result of condensation, evaporation, and diffusion of materials during the sintering process at the given sintering parameters [56]. Interestingly, fully formed adhesion and excellent grain refinement between the matrix and the particulates are well revealed in Figs. 1g and 2h and i sintered at higher temperature and heating rate. However,

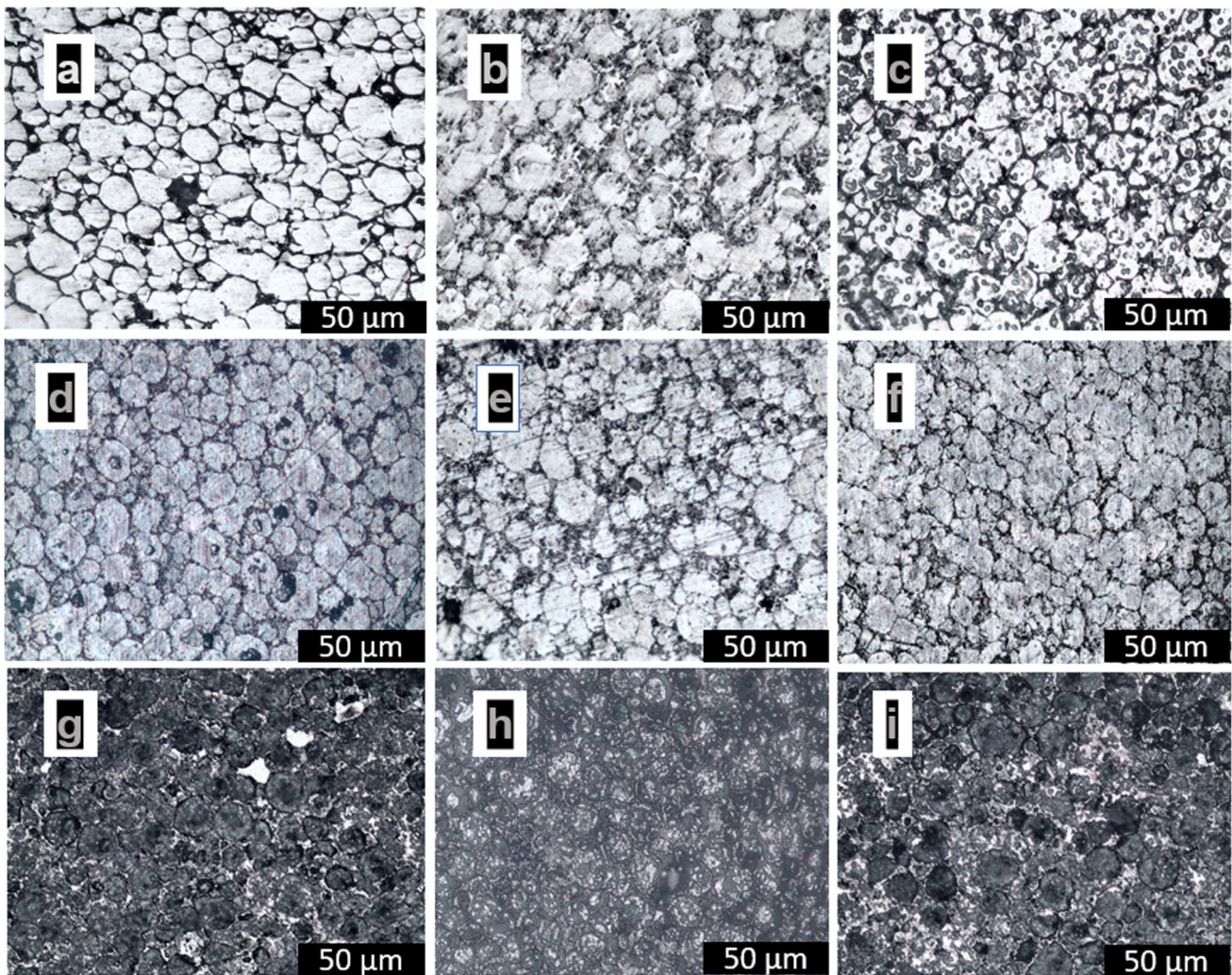


Fig. 1 The optical microstructure of sintered MgAZ91D-4wt%AlN-4wt%Y₂O₃-4wt%VB at varying sintering processing parameters

Fig. 2 The XRD phases of the sintered samples

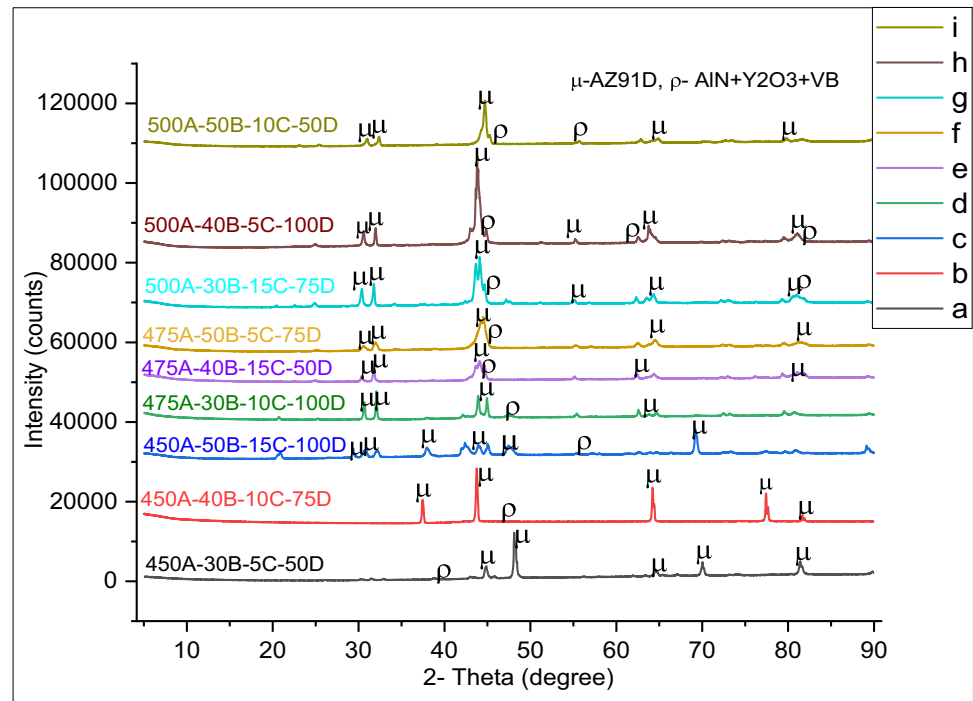


Fig. 1h that was sintered at 500 °C of temperature, 40 MPa pressure, dwell time of 5 min, and 100 °C/min heating rate is seen to pose the full neck growth with no vivid pores or cavities. This, in turn, means that full densification and strong material bonding were achieved at a higher sintering temperature and heating rate. Also, the sintering parameters employed to develop the samples in Fig. 1g, h, and i helped in enhancing the particle diffusion and wettability along the grain boundaries and thereafter improved the bonding structure and the properties of the composite.

It is imperative to state that the results obtained in this research affirmed the potential of the sintering route to fabricate a fully dense composite having input the right parameters. This is evidenced by the even dispersion of the hybrid AlN + Y₂O₃ + VB in the MgAZ91D matrix with enhanced interfacial bonding integrity. This improved bonding structure as experienced at higher sintering temperature and heating rate resulted in a void-free microstructure in the sintered materials. Hence, the stable positioning of the reinforced materials in the Mg matrix which depicted a strong adhesion will retard indentation compared to the unreinforced matrix. Additionally, the grain size distribution of the sintered samples is shown in Table 3 as obtained using the ImageJ software. The outcome of the result shows that the sintered composite at a lower temperature are having a higher grain size unlike the ones at a lower sintered temperature. For instance, the lowest grain size distribution of 17.68 μm was seen at 500A, 50B, 10C, and 100D while the highest grain distribution of 46 μm was seen at 450A, 50B, 15C, and 100D. This is another indication that higher temperature enhances the

Table 3 The grain size distribution of the sintered samples

Experiment samples	Grain size (μm)
a. (450A 30B 5C 50D)	41.01
b. (450A 40B 10C 75D)	39.88
c. (450A 50B 15C 100D)	46.06
d. (475A 30B 10C 100D)	30.64
e. (475A 40B 15C 50D)	22.17
f. (475A 50B 5C 75D)	24.11
g. (500A 30B 15C 75D)	20.35
h. (500A 40B 5C 100D)	17.68
i. (500A 50B 10C 50D)	19.72

refining of grain sizes along the grain boundaries by mitigating grain growth. The outcome of this work is similar to the research done by [1].

3.2 XRD

Figure 2 and Table 4 present the crystalline phase observed in the developed sintered composite based on the design of the parametric process. The XRD pattern was analyzed to examine the phase composition and to check the possible formation of any intermetallic compound. As observed on the plot, no intermetallic compound was formed even at a minimal negligible quantity, but the visibility of strong bonding among the composites is a result of the wettability between the AZ91D and the 4wt% AlN-4wt% Y₂O₃-4wt% VB. The peak intensity of the Magnesium AZ91D as the major phase

Table 4 The crystallite size of the nano hybrid magnesium composite at different optimized conditions

Experiment samples	Crystallite size (nm)
a. (450A 30B 5C 50D)	11.03
b. (450A 40B 10C 75D)	9.59
c. (450A 50B 15C 100D)	16.05
d. (475A 30B 10C 100D)	10.25
e. (475A 40B 15C 50D)	12.32
f. (475A 50B 5C 75D)	9.42
g. (500A 30B 15C 75D)	9.04
h. (500A 40B 5C 100D)	8.87
i. (500A 50B 10C 50D)	12.67

was prominently seen in all the materials, and it has the highest intensity. Precisely, the highest peak intensity of the AZ91D matrix and the reinforcement were obtained with the material sintered at the temperature of 500 °C, 40 MPa of pressure, 5 min of holding time, and 100 °C/min of heating rate. The peaks of the reinforcing phase were observed with lower intensity due to the quantity (weight percentage) inclusion. Despite the formation of the composite materials in all the optimized designs as seen by the peak intensity, the nature of the crystallite and texture size is determined by the optimized parameters and the incorporated reinforcement [1, 57]. These phases change the refinement of the grain structure and the crystallite size which in turn influences the entire properties of the materials and reduces the intensity of the AZ91D. In this research, the finer crystallite size of about 8.8687 nm was formed at a higher temperature of 500 °C and 100 °C/min heating rate. However, the crystallite size for all the optimized sintered samples was in the range of 8 to 16 nm which depicted the absence or minimal grain growth during the sintering route. Table 4 displays the crystallite size at different sintered designs as calculated using the Scherrer formula in Eq. 4. The outcome of the XRD is an indication that the spark plasma sintering route can be used conveniently to successfully fabricate a hybrid composite of MgAZ91D-4wt%AlN-4wt% Y₂O₃-4wt%VB.

3.3 The effect of the sintering parameters on the relative density

Table 5 presents the result of the relative density, experimental density, and the percentage porosity that was derived using Archimedes’ principle based on the L9 orthogonal array design of the parametric process. Tables 6 and 7 reveal the response for the mean and the response for the signal-to-noise ratio (S/N ratio) of the relative density. Figs. 3 and 4 represent the main effect plots for the relative density and the signal-to-noise ratio. From the plot in Fig. 3, it can

Table 5 Experimental data of the sintered parameters for density, relative density, and porosity

Experimental sample	Experimental density (g/cm ³)	Relative density	Porosity (%)
a. (450A 30B 5C 50D)	1.80 ± 0.79	95.79	4.21
b. (450A 40B 10C 75D)	1.80 ± 0.99	95.79	4.21
c. (450A 50B 15C 100D)	1.79 ± 0.42	95.63	4.37
d. (475A 30B 10C 100D)	1.81 ± 0.50	96.50	3.52
e. (475A 40B 15C 50D)	1.80 ± 0.90	95.79	4.21
f. (475A 50B 5C 75D)	1.82 ± 0.41	96.96	3.04
g. (500A 30B 15C 75D)	1.84 ± 0.22	98.19	1.81
h. (500A 40B 5C 100D)	1.85 ± 0.07	98.45	1.55
i. (500A 50B 10C 50D)	1.83 ± 0.13	97.45	2.35

Table 6 Response table for means of relative density

Level	Temperature (°C)	Pressure (MPa)	Dwell time (min)	Heating rate (°C/min)
1	95.77	96.83	97.07	96.46
2	96.47	96.77	96.68	97.02
3	98.10	96.75	96.59	96.86
Delta	2.32	0.08	0.48	0.55
Rank	1	4	3	2

be inferred that the optimal density is achieved at 500 °C, 30 MPa of pressure, 5 min of dwell time, and 75 °C/min. In Fig. 4, “larger is better” was selected to evaluate the signal-to-noise ratio of the relative density, and 500 °C, 30 MPa of pressure, 5 min of dwell time, and 75 °C/min gave the obvious excellent density. In all, the response outcome as seen in Tables 6 and 7 depicted that the temperature is the most significant parameter among the sintering parameters as it ranked 1.

At this point, it is important to state that the increase in relative density with increasing temperature is a function

Table 7 Response table for signal to noise ratios of relative density

Level	Temperature(°C)	Pressure (MPa)	Dwell time (min)	Heating rate (°C/min)
1	39.62	39.72	39.74	39.69
2	39.69	39.71	39.71	39.74
3	39.83	39.71	39.70	39.72
Delta	0.21	0.01	0.04	0.05
Rank	1	4	3	2

Fig. 3 Main effect for means of relative density

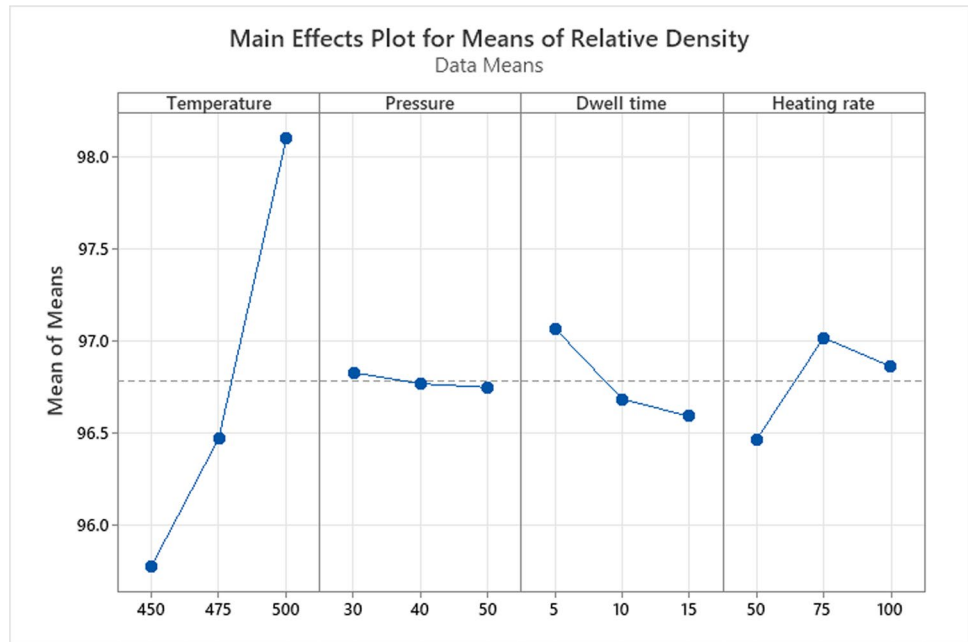
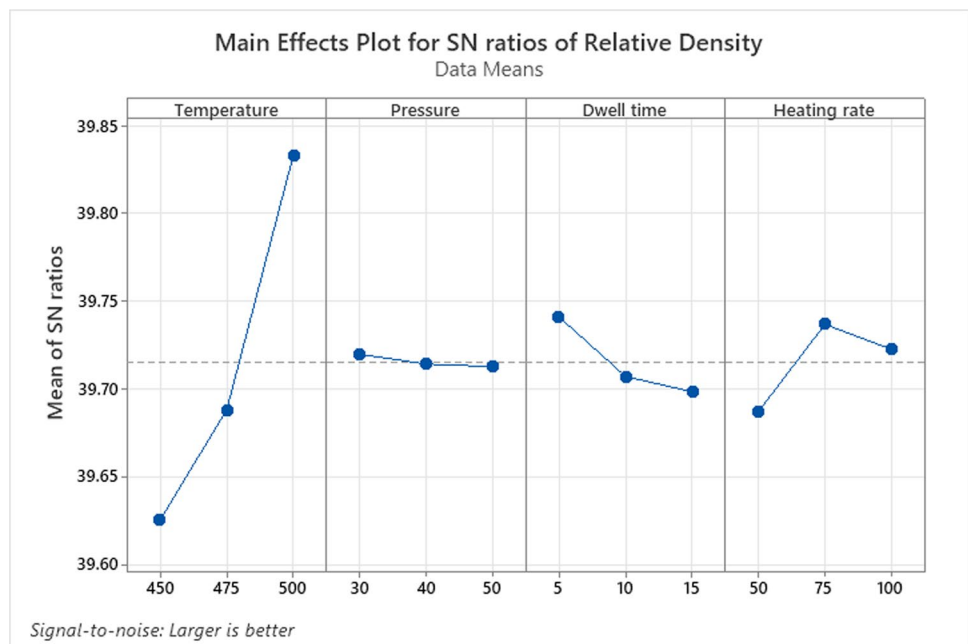


Fig. 4 Main effects plot for SN ratio of relative density



of the improved and even diffusivity of the nano reinforcing particulates in the Mg matrix which in turn mitigates again the formation of porosity for the Mg-4AlN-4Y₂O₃-4VB composite. Obviously, porosity cannot be completely eradicated but can be reduced to the barest minimum, and hence, 1.55% was achieved as shown in Table 5. This is a shred of evidence that the SPS technique is a reliable route to developing highly dense materials with less porosity. The observed low density in some of the sintered parameters can be ascribed to the voids formed in between the particulates arising from diffusion deficiency [1].

To further understand the effect of the sintered parameters on the relative density, the experimental design was subjected to the analysis of variance (ANOVA) as seen in Table 8. The one-way ANOVA model is often carried out at a 95% confidence interval with a 5% significance level. Hence, the *P*-value observed in this novel research for all the parametric processes confirmed temperature with a *P*-value of 0.007 as the only statistically significant variable that contributed uniquely to the high densification of the developed composite with about 90.63% contribution. This shows that only the sintering temperature possessed a *P*-value that

Table 8 Analysis of variance (ANOVA) results in relation to the relative density

Source	Degree of freedom (DF)	Sum of squares (SS)	Mean of squares (MS)	F-value	P-value	Contribution or R-Sq. (%)
Temperature (A)	2	8.529	4.265	29.030	0.007	90.631
Pressure (B)	2	0.010	0.005	0.001	0.997	0.111
Dwell time (C)	2	0.383	0.191	0.132	0.883	4.072
Heating rate (D)	2	0.488	0.244	0.160	0.852	5.190
Error	6	7.058	1.176	–	–	75.000
Total	8	9.412				100

Table 9 Experimental data of the sintered parameters for the microhardness

Experimental sample	Microhardness (HV)
a. (450A 30B 5C 50D)	76 ± 0.12
b. (450A 40B 10C 75D)	80 ± 0.16
c. (450A 50B 15C 100D)	79 ± 0.13
d. (475A 30B 10C 100D)	92 ± 0.32
e. (475A 40B 15C 50D)	88 ± 0.24
f. (475A 50B 5C 75D)	97 ± 0.37
g. (500A 30B 15C 75D)	102 ± 0.41
h. (500A 40B 5C 100D)	106 ± 0.45
i. (500A 50B 10C 50D)	100 ± 0.38

is lesser than the 5% confidence interval. Among the non-significant factors, the pressure was seen with the most negligible P-value of 0.997 with a 0.11% contribution.

3.4 The effect of the sintering parameters on the microhardness

The experimental data of the sintered parameters for the hardness is presented in Table 9 based on the Taguchi design of the orthogonal array. This experiment was conducted to evaluate the effect of the parameters on the strengthening mechanism of the composite. Fig. 5 displays the main parametric effect on the resultant hardness while the confirmatory effect based on the ratio of signal-to-noise is shown in Fig. 6. As shown in Table 9, samples sintered at the highest temperature of 500 °C had the best microhardness property. The improvement of the hardness can be ascribed to the inclusion of the uniformly distributed ternary reinforcing particulates, and the full densification achieved at a high temperature which enhances the deformation of the Mg alloy during the indentation process or rather aided the transfer of the load bearing from the Mg matrix.

Fig. 5 Main effect for means of microhardness

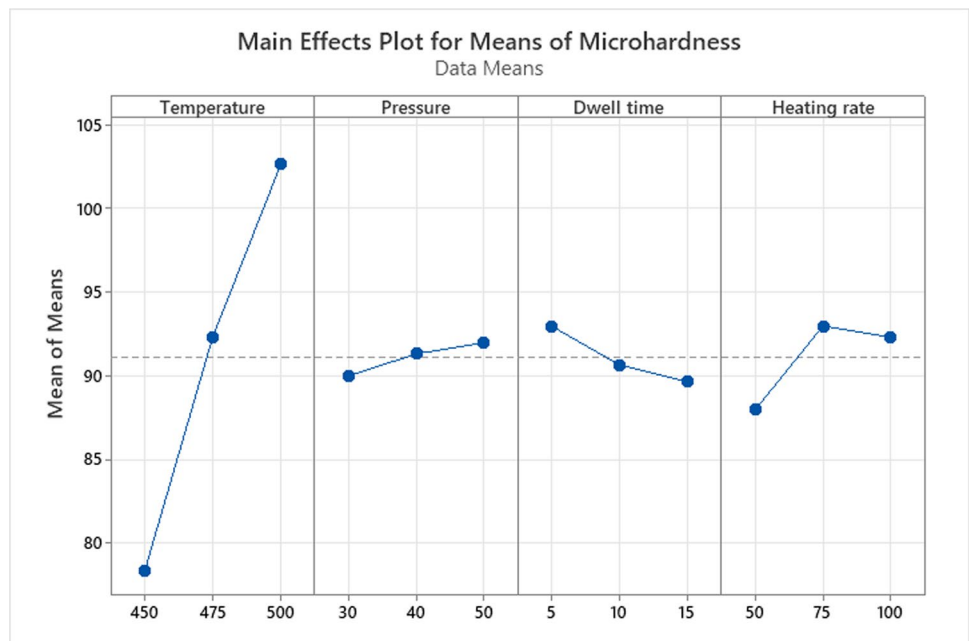


Fig. 6 Mean effect plot for SN ratios of microhardness

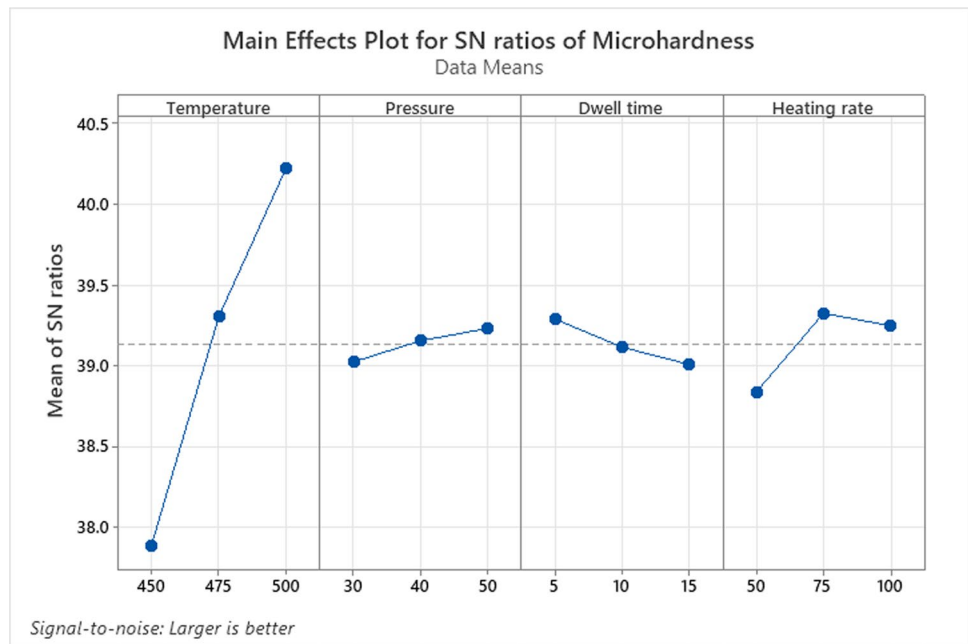


Table 10 Response table for means of microhardness

Level	Temperature (°C)	Pressure (MPa)	Dwell time (min)	Heating rate (°C/min)
1	78.33	90.00	93.00	88.00
2	92.33	91.33	90.67	93.00
3	102.67	92.00	89.67	92.33
Delta	24.33	2.00	3.33	5.00
Rank	1	4	3	2

Table 11 Response table for signal-to-noise ratios of microhardness

Level	Temperature (°C)	Pressure (MPa)	Dwell time (min)	Heating rate (°C/min)
1	37.88	39.02	39.29	38.84
2	39.30	39.15	39.11	39.32
3	40.23	39.23	39.00	39.24
Delta	2.35	0.21	0.28	0.49
Rank	1	4	3	2

At high temperatures, the pore spaces were eliminated, and grain growth was prevented which in turn improved the hardness and densification of the composite materials [1, 58].

As shown in Fig. 5 which is the main effect plot of the means of the microhardness, there is an increase in hardness from 78.33 to 102.67 HV when the temperature progresses from 450 to 500 °C. From the plot evaluation in Fig. 6, it can be asserted that the optimal hardness is obtained at 500 °C, 50 MPa of pressure, 5 min of dwell time, and 75 °C/min. The “larger is better” was chosen to examine the signal-to-noise ratio of the microhardness, and 500 °C, 50 MPa of pressure, 5 min of dwell time, and 75 °C/min revealed the best optimal value for the hardness. In summary, the response data value as shown in Tables 10 and 11 depicted that the temperature is the most significant parameter among the process variables as it ranked 1 followed by the heating rate (2), dwell time (3), and then pressure as 4.

The ANOVA results of the hardness which is a function of the variable factors are presented in Table 12. As

observed, the factor of temperature has a *P*-value of 0.004 with 92.94% highest contribution. This depicted that temperature contributed immensely and served as the major factor that influences the hardness of the materials. The temperature is the only variable that significantly influences the hardness as it possesses a value that is lesser than the maximum significant level of 5%. Hence, in this study, other variables such as the pressure, dwell time, and heating rate were considered less significant.

3.5 The effect of the sintering parameters on the nanohardness

The result of the nanohardness that was measured using the Berkovich diamond nanoindenter at an applied load of 100 mN is displayed in Table 13. In addition, the response means of the hardness and its signal-to-noise ratio are presented in Tables 14 and 15, respectively. Likewise, the plot of the main effect mean of the factors and the corresponding main effect of the S/N ratio

Table 12 ANOVA results in relation to the microhardness

Source	Degree of freedom (DF)	Sum of squares (SS)	Mean of squares (MS)	F-value	P-value	Contribution or R-Sq. (%)
Temperature (A)	2	894.89	447.440	39.480	0.004	92.940
Pressure (B)	2	6.222	3.111	0.021	0.981	0.651
Dwell time (C)	2	17.56	8.778	0.062	0.946	1.820
Heating rate (D)	2	44.22	22.111	0.141	0.868	4.591
Error	6	722.167	120.362	–	–	75
Total	8	962.89	–	–	–	100

Table 13 Experimental data of the sintered parameters for the nanohardness

Experimental sample	Nanohardness (GPa)
a. (450A 30B 5C 50D)	0.5
b. (450A 40B 10C 75D)	1.6
c. (450A 50B 15C 100D)	0.8
d. (475A 30B 10C 100D)	1.3
e. (475A 40B 15C 50D)	1.1
f. (475A 50B 5C 75D)	1.5
g. (500A 30B 15C 75D)	2.5
h. (500A 40B 5C 100D)	2.8
i. (500A 50B 10C 50D)	1.9

Table 14 Response table for means of nanohardness

Level	Temperature (°C)	Pressure (MPa)	Dwell time (min)	Heating rate (°C/min)
1	0.9667	1.4333	1.6000	1.1667
2	1.3000	1.8333	1.6000	1.8667
3	2.4000	1.4000	1.4667	1.6333
Delta	1.4333	0.4333	0.1333	0.7000
Rank	1	3	4	2

are given in Figs. 7 and 8. An increase in nanohardness is significantly observed with an increase in temperature reaching a maximum value of 2.4 GPa at 500 °C as illustrated in Fig. 7. This improvement in nanohardness can be ascribed to the strong interfacial bonding atomic structure with resultant high densification as a function of the increasing sintering temperature. This material’s temperature retarded against the dislocation movement and decrease the dislocation density. According to [37], when the sintering temperature is increased, the solid-state diffusion between the matrix and the reinforcing phase is often enhanced during the consolidation process which in turn improves the neck growth formation. Thus,

Table 15 Response table for signal to noise ratios of nanohardness

Level	Temperature (°C)	Pressure (MPa)	Dwell time (min)	Heating rate (°C/min)
1	–1.2921	1.4057	2.1481	0.1274
2	2.2095	4.6178	3.9788	5.1877
3	7.4923	2.3862	2.2828	3.0946
Delta	8.7845	3.2121	1.8307	5.0602
Rank	1	3	4	2

the strong interparticle adhesion leads to an excellent nanohardness of the composite materials. Likewise, [1] reported somewhat similar to the current novel research in which an increase in pressure above 40 MPa, sintering time beyond 5 min, and heating rate above 75 °C/min resulted in a significant regression in the mechanical properties as shown in Fig. 7 and confirmed by the signal-to-noise ratio plot in Fig. 8. This is a piece of evidence that the optimal nanohardness can be achieved when the composite is sintered at 500 °C, 40 MPa, 5 min of sintering time, and 75 °C/min of heating rate.

The outcome of the ANOVA for the nanohardness is presented in Table 16. As illustrated, the variable of temperature has a P-value of 0.016 with a 74.64% contribution compared to the other parametric variables. This accounts for the temperature as the major significant influencer of the Pis considered significant to the material development when the P-value is below 0.05 significant level.

Interestingly, a remarkable difference occurs between the nanohardness and the microhardness behavior of materials. The nanohardness response of a material with a localized approach is estimated from the maximum peak load applied and the contact area of indentation within the grains; this gives a more accurate result as the elastic recovery of the material is duly catered for during the nanoindentation. Whereas, the microhardness behavior of a material is averaged from different grains at a large residual contact area.

Fig. 7 Main effect plot for means of nanohardness

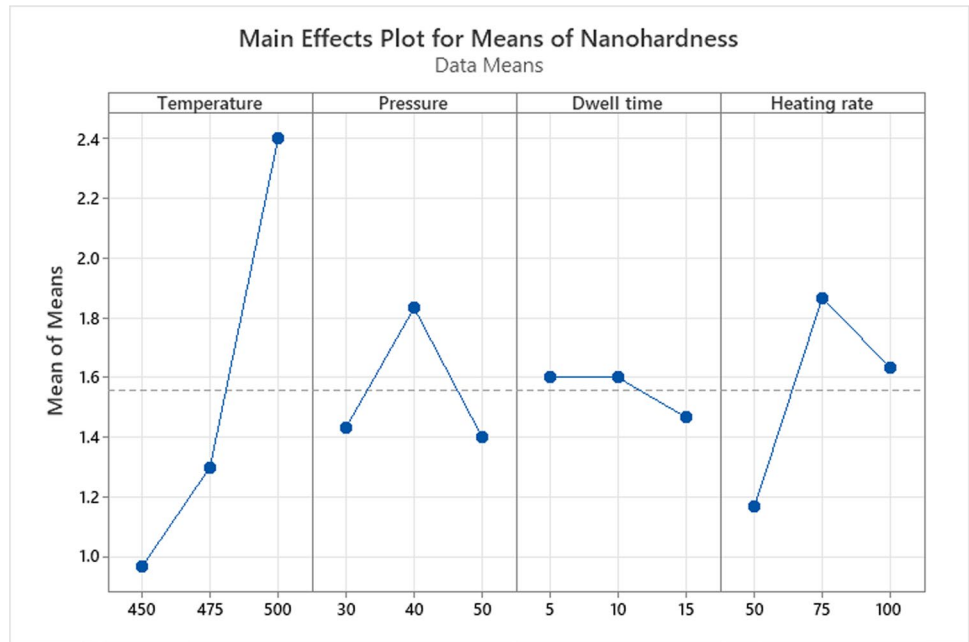


Fig. 8 Main effects plots for SN ratios of nanohardness

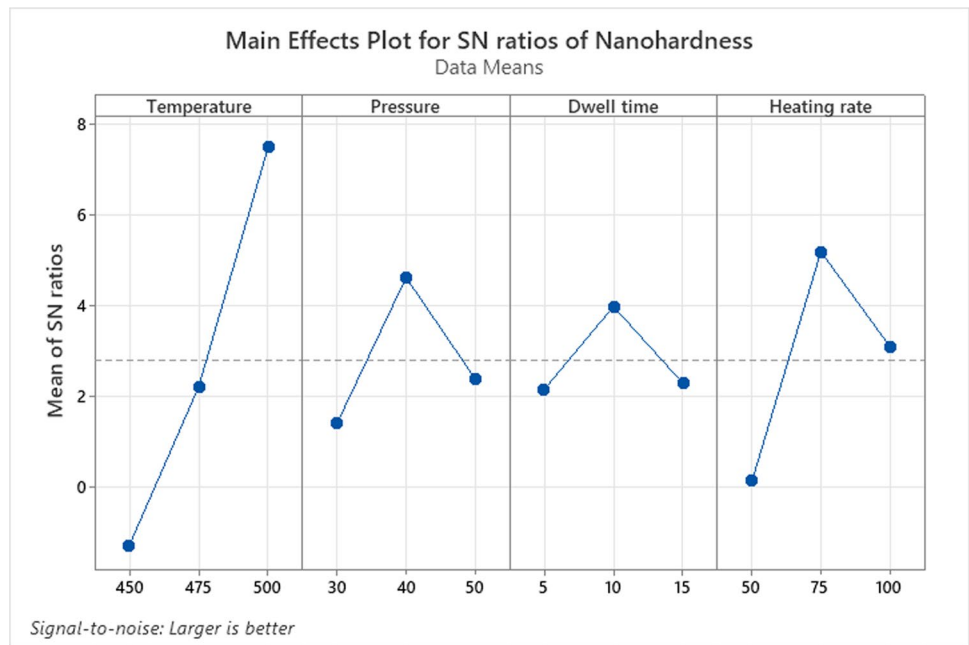


Table 16 ANOVA results in relation to the nanohardness

Source	Degree of freedom (DF)	Sum of squares (SS)	Mean of squares (MS)	F-value	P-value	Contribution or R-Sq. (%)
Temperature (A)	2	3.376	1.688	8.830	0.016	74.641
Pressure (B)	2	0.3489	0.174	0.251	0.786	7.710
Dwell time (C)	2	0.0356	0.748	0.020	0.977	0.791
Heating rate (D)	2	0.7622	0.381	0.611	0.575	16.863
Error	6	3.3917	0.391	–	–	74.911
Total	8	4.5222	–	–	–	100

4 Conclusion

In this research, a novel quaternary magnesium-based composite has been successfully fabricated via powder metallurgy of spark plasma sintering route. The optimization of the process parameters was carried out using the Taguchi design in MINITAB software version 19.1.1. In summary, the influence of temperature, sintering pressure, dwell time, and heating rate on the microstructure, density, relative density, porosity, hardness, and nanohardness was studied following the analysis by optimization. Hence, the following summations were reached:

1. AZ91D magnesium-based composite reinforced with quaternary AZ91D-4wt.%AlN-4wt.%Y₂O₃-4wt.%VB was fabricated successfully by a sintering process.
2. The microstructural evolution of the composite as revealed by the optical micrographs shows no occurrence of pore-space but uniformity in the distribution of the reinforcing materials. The strong adhesion bonding and interfacial diffusion that occurs between the two phases resulted in the neck formation mostly at a higher temperature of 500 °C.
3. The consolidation and solidification of AZ91D powder with 4wt.%AlN-4wt.%Y₂O₃-4wt.%VB using the sintering route amounted to nearly full densification of about 98.45%.
4. The crystallite grain size of the fabricated optimized samples decreases with an increase in temperature as the temperature is the main variable that influences the degree of grain refinement of the composite.
5. The sintering temperature was observed as the only parametric factor that significantly influence or contribute to the improvement of microhardness, nanohardness, and low porosity.
6. The outcome of the optimization depicted that the best optimal conditions for full densification can be achieved at 500 °C, 30 MPa of pressure, 5 min of dwell time, and 75 °C/min.

Funding There is no special grant for this research. However, necessary support was given by the Department of Chemical, Metallurgical, and Materials Engineering of Tshwane University of Technology, Pretoria, South Africa.

Data availability The data used in this research are not available publicly. However, it can be obtained from the authors once a justifiable request is made.

Code availability Not applicable.

Declarations

Ethics approval and consent to participate Not applicable.

Conflict of interest The authors declare no competing interests.

References

1. Ali M, Hussein MA, Al-Aqeeli N (2020) Optimization of spark plasma sintering parameters using the Taguchi method for developing Mg-based composites. *JOM* 72(3):1186–1194
2. Dey A, Pandey KM (2015) Magnesium metal matrix composites—a review. *Rev Adv Mater Sci* 42(1)
3. Del Campo R, Savoini B, Muñoz A, Monge MA, Garcés G (2014) Mechanical properties and corrosion behavior of Mg–HAP composites. *J Mech Behav Biomed Mater* 39:238–246
4. Kand AJT, Afaghi F, Tabrizi AT, Aghajani H, Kivrak HD (2021) Electrochemical evaluation of the hydroxyapatite coating synthesized on the AZ91 by electrophoretic deposition route. *Synth Sinter* 1(2):85–91
5. Zhou YJ, Jiang AY, Liu JX (2013) The effect of sintering temperature to the microstructure and properties of AZ91 magnesium alloy by powder metallurgy. In *Applied Mechanics and Materials* (Vol. 377, pp. 250–254). Trans Tech Publications Ltd
6. Meng G, Yue TM, Lin X, Yang H, Xie H, Ding X (2015) Laser surface forming of AlCoCrCuFeNi particle reinforced AZ91D matrix composites. *Opt Laser Technol* 70:119–127
7. Yu W, Wang X, Zhao H, Ding C, Huang Z, Zhai H, Guo Z, Xiong S (2017) Microstructure, mechanical properties and fracture mechanism of Ti2AlC reinforced AZ91D composites fabricated by stir casting. *J Alloy Compd* 702:199–208
8. Xiong Y, Zhang MX (2014) The effect of cold sprayed coatings on the mechanical properties of AZ91D magnesium alloys. *Surf Coat Technol* 253:89–95
9. Zhang L, Wang Q, Liao W, Guo W, Ye B, Li W, Jiang H, Ding W (2017) Effects of cyclic extrusion and compression on the microstructure and mechanical properties of AZ91D magnesium composites reinforced by SiC nanoparticles. *Mater Charact* 126:17–27
10. Liu T, Li Y, Zhang Y, Zhao M, Wen Z, Zhang L (2021) A biodegradable, mechanically tunable micro-arc oxidation AZ91D-based composite implant with calcium phosphate/chitosan coating promotes long-term bone tissue regeneration. *Biotechnol J* 16(10):2000653
11. Khatkar SK, Verma R, Kharb SS, Thakur A, Sharma R (2021) Optimization and effect of reinforcements on the sliding wear behavior of self-lubricating AZ91D-SiC-Gr hybrid composites. *SILICON* 13(5):1461–1473
12. Rončević IŠ, Grubač Z, Metikoš-Huković M (2014) Electrodeposition of hydroxyapatite coating on AZ91D alloy for biodegradable implant application. *Int J Electrochem Sci* 9:5907–5923
13. Ponappa K, Aravindan S, Rao PV (2013) Influence of Y₂O₃ particles on mechanical properties of magnesium and magnesium alloy (AZ91D). *J Compos Mater* 47(10):1231–1239
14. Matta AK, Koka NSS, Devarakonda SK (2020) Recent studies on particulate reinforced AZ91 magnesium composites fabricated by stir casting—a review. *J Mech Energy Eng* 4
15. Casati R, Vedani M (2014) Metal matrix composites reinforced by nano-particles—a review. *Metals* 4(1):65–83

16. Sankaranarayanan S, Habibi MK, Jayalakshmi S, Jia Ai K, Almajid A, Gupta M (2015) Nano-AlN particle reinforced Mg composites: microstructural and mechanical properties. *Mater Sci Technol* 31(9):1122–1131
17. Zhang H, Zhao Y, Yan Y, Fan J, Wang L, Dong H, Xu B (2017) Microstructure evolution and mechanical properties of Mg matrix composites reinforced with Al and nano SiC particles using spark plasma sintering followed by hot extrusion. *J Alloy Compd* 725:652–664
18. Shen MJ, Wang XJ, Ying T, Wu K, Song WJ (2016) Characteristics and mechanical properties of magnesium matrix composites reinforced with micron/submicron/nano SiC particles. *J Alloy Compd* 686:831–840
19. Shang J, Ke L, Liu F, Lv F, Xing L (2019) Aging behavior of nano SiC particles reinforced AZ91D composite fabricated via friction stir processing. *J Alloy Compd* 797:1240–1248
20. Zhao R, Pei J, Du W, Zhao Z, Zhang L, Gao J, Bai P, Tie D (2021) Fabrication of magnesium-coated graphene and its effect on the microstructure of reinforced AZ91 magnesium-matrix composites. *Adv Compos Hybrid Mater* 1–9
21. Raja KS, Kumar UM, Mathivanan S, Ganesan S, Arunkumar T, Hemanandh J, Kumar JS (2021) Mechanical and microstructural properties of graphene reinforced magnesium composite. *Mater Today Proc* 44:3571–3574
22. Saberi A, Bakhsheshi-Rad HR, Karamian E, Kasiri-Asgarani M, Ghomi H (2020) Magnesium-graphene nano-platelet composites: corrosion behavior, mechanical and biological properties. *J Alloy Compd* 821:153379
23. Tun KS, Gupta M (2007) Improving mechanical properties of magnesium using nano-yttria reinforcement and microwave-assisted powder metallurgy method. *Compos Sci Technol* 67(13):2657–2664
24. Hassan SF, Tun KS, Gupta M (2011) Effect of sintering techniques on the microstructure and tensile properties of nano-yttria particulates reinforced magnesium nanocomposites. *J Alloy Compd* 509(11):4341–4347
25. Pc E, Radhakrishnan G, Emarose S (2021) Investigation into physical, microstructural and mechanical behaviour of titanium dioxide nanoparticle reinforced magnesium composite. *Mater Technol* 36(10):575–584
26. Rahmani K, Majzoobi GH, Sadooghi A, Kashfi M (2020) Mechanical and physical characterization of Mg-TiO₂ and Mg-ZrO₂ nanocomposites produced by hot-pressing. *Mater Chem Phys* 246:122844
27. Sahoo SK, Sahoo BN, Panigrahi SK (2020) Effect of in-situ submicron sized TiB₂ reinforcement on microstructure and mechanical properties in ZE41 magnesium matrix composites. *Mater Sci Eng A* 773:138883
28. Xiao P, Gao Y, Yang C, Liu Z, Li Y, Xu F (2018) Microstructure, mechanical properties and strengthening mechanisms of Mg matrix composites reinforced with in situ nanosized TiB₂ particles. *Mater Sci Eng A* 710:251–259
29. Aydin F, Sun Y (2018) Investigation of wear behaviour and microstructure of hot-pressed TiB₂ particulate-reinforced magnesium matrix composites. *Can Metall Q* 57(4):455–469
30. Borodianskiy K, Zinigrad M (2016) Modification performance of WC nanoparticles in aluminum and an Al-Si casting alloy. *Metall Mater Trans B* 47:1302–1308. <https://doi.org/10.1007/s11663-016-0586-0>
31. Pal A, Poria S, Sutradhar G, Sahoo P (2018) Tribological behavior of Al-WC nano-composites fabricated by ultrasonic cavitation assisted stir-cast method. *Mater Res Express* 5(3):036521
32. Karuppusamy P, Lingadurai K, Sivananth V, Arulkumar S (2021) A study on mechanical properties of tungsten carbide reinforced magnesium metal matrix composites for the application of piston. *Int J Light Mater Manuf* 4(4):449–459
33. Paramsothy M, Tan XH, Chan J, Kwok R, Gupta M (2012) Si₃N₄ nanoparticle addition to concentrated magnesium alloy AZ81: enhanced tensile ductility and compressive strength. *Int Sch Res Not* 2012
34. Balikai A, Adarsha H, Keshavamurthy R (2022) Microstructure and nanoindentation response of Si₃N₄-reinforced magnesium-based composite synthesized by powder metallurgy route. *J Inst Eng (India) Series D* 1–13
35. Hussein MA, Suryanarayana C, Arumugam MK, Al-Aqeeli N (2015) Effect of sintering parameters on microstructure, mechanical properties and electrochemical behavior of Nb–Zr alloy for biomedical applications. *Mater Des* 83:344–351
36. Kumar PS, Ponappa K, Udhayasankar M, Aravindkumar B (2017) Dry sliding wear and mechanical characterization of Mg based composites by uniaxial cold press technique. *Arch Metall Mater*
37. Singh LK, Bhaduria A, Jana S, Laha T (2018) Effect of sintering temperature and heating rate on crystallite size, densification behaviour and mechanical properties of Al-MWCNT nanocomposite consolidated via spark plasma sintering. *Acta Metallurgica Sinica (English Letters)* 31(10):1019–1030
38. Aravindan S, Rao PV, Ponappa K (2015) Evaluation of physical and mechanical properties of AZ91D/SiC composites by two step stir casting process. *J Magnes Alloys* 3(1):52–62
39. Huang SJ, Abbas A (2020) Effects of tungsten disulfide on microstructure and mechanical properties of AZ91 magnesium alloy manufactured by stir casting. *J Alloy Compd* 817:153321
40. Dinaharan I, Akinlabi ET (2018) Low cost metal matrix composites based on aluminum, magnesium and copper reinforced with fly ash prepared using friction stir processing. *Compos Commun* 9:22–26
41. Sunil BR, Reddy GPK, Patle H, Dumpala R (2016) Magnesium based surface metal matrix composites by friction stir processing. *J Magnes alloys* 4(1):52–61
42. Riquelme A, Rodrigo P, Escalera-Rodriguez MD, Rams J (2021) Evaluation of the wear resistance and corrosion behavior of laser cladding al/sic metal matrix composite coatings on ze41 magnesium alloy. *Coatings* 11(6):639
43. Park Y, Cho K, Park I, Park Y (2011) Fabrication and mechanical properties of magnesium matrix composite reinforced with Si coated carbon nanotubes. *Procedia Eng* 10:1446–1450
44. Chen B, Yin KY, Lu TF, Sun BY, Dong Q, Zheng JX, Lu C, Li ZC (2016) AZ91 magnesium alloy/porous hydroxyapatite composite for potential application in bone repair. *J Mater Sci Technol* 32(9):858–864
45. Meenashisundaram GK, Gupta M (2014) Low volume fraction nano-titanium particulates for improving the mechanical response of pure magnesium. *J Alloy Compd* 593:176–183
46. Paramsothy M, Tan XH, Chan J, Kwok R, Gupta M (2012) Si₃N₄ nanoparticle addition to concentrated magnesium alloy AZ81: enhanced tensile ductility and compressive strength. *Int Sch Res Not* 2012
47. Dodi E, Balak Z, Kafashan H (2022) Oxidation-affected zone in the sintered ZrB₂–SiC–HfB₂ composites. *Synth Sinter* 2(1):31–36
48. Cohen S, Ratzker B, Sokol M, Kalabukhov S, Frage N (2018) Polycrystalline transparent magnesium aluminate spinel processed by a combination of spark plasma sintering (SPS) and hot isostatic pressing (HIP). *J Eur Ceram Soc* 38(15):5153–5159
49. Shahbazi H, Shokrollahi H, Tataei M (2018) Gel-casting of transparent magnesium aluminate spinel ceramics fabricated by spark plasma sintering (SPS). *Ceram Int* 44(5):4955–4960
50. Wang S, Huang Y, Yang L, Zeng Y, Hu Y, Zhang X, Sun Q, Shi S, Meng G, Hort N (2021) Microstructure and mechanical properties of Mg-3Sn-1Ca reinforced with AlN nano-particles. *J Magnes Alloys*
51. Yang C, Zhang B, Zhao D, Lü H, Zhai T, Liu F (2016) Microstructure and mechanical properties of AlN particles in situ reinforced Mg matrix composites. *Mater Sci Eng A* 674:158–163

52. Katsarou L, Mounib M, Lefebvre W, Vorozhtsov S, Pavese M, Badini C, Molina-Aldareguia JM, Jimenez CC, Prado MTP, Dieringa H (2016) Microstructure, mechanical properties and creep of magnesium alloy Elektron21 reinforced with AlN nanoparticles by ultrasound-assisted stirring. *Mater Sci Eng A* 659:84–92
53. Falcon-Franco L, Rosales I, García-Villarreal S, Curiel FF, Arizmendi-Morquecho A (2016) Synthesis of magnesium metallic matrix composites and the evaluation of aluminum nitride addition effect. *J Alloy Compd* 663:407–412
54. Ma L, Zhang J, Yue G, Zhang H, Zhou L, Zhang H (2016) Improvement and application of Y2O3 directional solidification crucible. *Chin J Aeronaut* 29(2):554–559
55. Tekoğlu E, Ağaoğulları D, Mertdinç S, Paksoy AH, Öveçoğlu ML (2018) Microstructural characterizations and mechanical properties of NbB2 and VB particulate-reinforced eutectic Al-12.6 wt% Si composites via powder metallurgy method. *Adv Powder Technol* 29(9):2070–208
56. Ujah CO, Popoola API, Popoola OM, Aigbodion VS (2019) Optimisation of spark plasma sintering parameters of Al-CNTs-Nb nano-composite using Taguchi design of experiment. *Int J Adv Manuf Technol* 100(5):1563–1573
57. Stanford N, Atwell D, Beer A, Davies C, Barnett MR (2008) Effect of microalloying with rare-earth elements on the texture of extruded magnesium-based alloys. *Scripta Mater* 59(7):772–775
58. Salamon D, Shen Z (2008) Pressure-less spark plasma sintering of alumina. *Mater Sci Eng A* 475(1–2):105–107

Publisher's note Springer Nature remains neutral with regard to jurisdictional claims in published maps and institutional affiliations.

Springer Nature or its licensor (e.g. a society or other partner) holds exclusive rights to this article under a publishing agreement with the author(s) or other rightsholder(s); author self-archiving of the accepted manuscript version of this article is solely governed by the terms of such publishing agreement and applicable law.